Deformation and wake of a flexible rotor in water

Ahmed S Eldemerdash, T Leweke

Deformation and wake of a flexible rotor in water

Deformation and wake of a flexible rotor in water

A S Eldemerdash, T Leweke
Aix-Marseille Université, CNRS, Centrale Marseille, IRPHE, 13384 Marseille, France
E-mail: eldemerdash@irphe.univ-mrs.fr

Abstract. In this paper, we study experimentally the fluid-structure interaction of a simplified small-scale rotor operating in a water channel. The rotor consists of a single untwisted rectangular blade and is tested with various pitch angles at different rotation speeds and free stream velocities. Flapwise blade deformations are measured using image processing, and flow fields are obtained by Particle Image Velocimetry. The blade exhibits extreme downstream and upstream bending at high negative and positive pitch angles, respectively. In addition, for negative pitch angles, unsteady flapwise fluctuations are observed, accompanied by large-scale recirculation zones. These zones are formed and shed periodically behind the rotor, resembling the dynamics of the Vortex Ring State known for helicopters in steep descent. The induced axial velocity near the blade tip changes direction from upstream to downstream, in accordance with the bending direction, reaching values that exceed twice the free-stream velocity in extreme bending conditions. The blade deformation has a strong dependence on the tip speed ratio for low pitch angles, and a more pronounced dependence on the tip Reynolds number for high pitch angles. Results for a two-bladed rotor are also shown and compared to the behaviour observed for a single blade.

1. Introduction

The blades of a rotor often exhibit some degree of flexibility, due to their material properties or sheer size. Examples include drones, helicopters and large wind turbines. Blade flexibility can be detrimental, since overbending or undesirable torsion of the blades can not only lead to a degradation of the rotor performance [1], but may also cause permanent damage to the blade structure. In addition, undesired instabilities can arise from the fluid-structure interaction: static divergence, classical flutter or luffing [2, 3]. Flexibility can, on the other hand, also be beneficial. It can be used to increase the mechanical strength of a rotor or expand its operational range [4, 5, 6, 7]. In a recent study, Cognet *et al.* [5] investigated experimentally the performance of a small-scale wind turbine rotor with flexible blades. Compared to the case with rigid blades, it showed a higher efficiency over a wide range of operating conditions. This performance enhancement was explained by the passive change of the pitch angle, induced by the fluid forces, towards a more optimal value.

For rotors operating in a liquid, the fluid forces acting on the blades are significantly higher compared to lower-density media such as air, implying the possibility of larger deformations. Underwater rotors have been studied for various applications, including the propulsion of AquaUAVs [8, 9, 10] and energy conversion via Marine Hydrokinetic Turbines [11, 12]. In the latter context, passively adaptive flexible blades were found to reduce the load fluctuations caused by waves, which is beneficial for the reliability and durability of the turbine [13]. Similarly

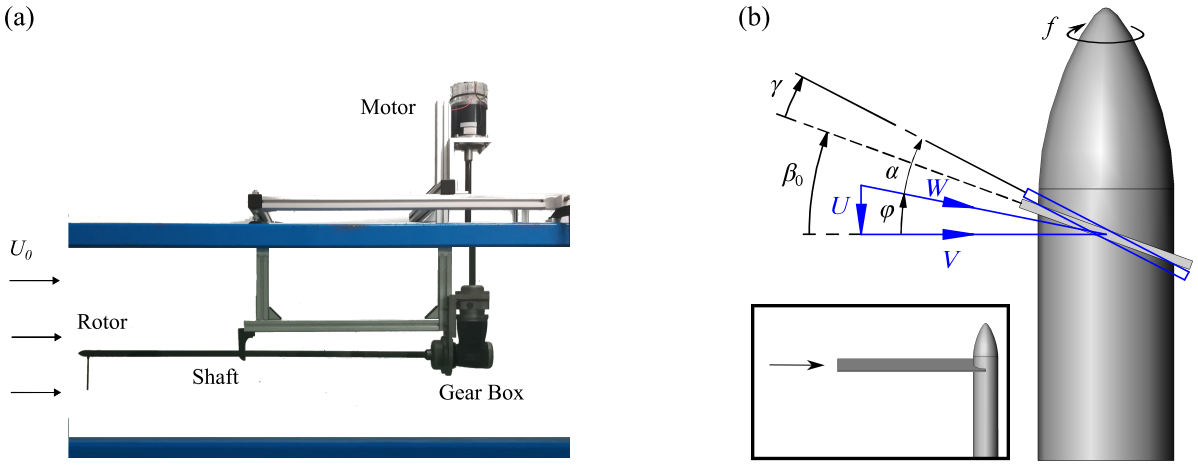

Figure 1. (a) Experimental set-up: water channel test section (side view). (b) Blade angles and relative velocities. β_0: pitch, γ: twist, φ: flow angle, α: angle of attack.

to wind turbines in a wind farm, marine current turbines operating in array configurations are also subjected to wake effects [14, 15].

Rotors can be moderately flexible, where the blades are able to sustain their own weight; highly flexible [6], where the blades exhibit strong deformation at rest due to their weight; or fully flexible [3], when the blades have very low stiffness in bending, torsion and also in the chordwise direction. In the following, we present results from an experimental study of moderately flexible rotors in water, which can nevertheless exhibit significant deformations. The rotors have a simple generic geometry: either one or two rectangular blades of constant thickness and without twist. This study is intended to provide a qualitative survey of the deformation behaviour of a flexible rotor in a high-density fluid in various regimes of operation, and to establish a link with the corresponding wake behaviour.

The experimental set-up and the methods used for measuring the blade deformations and flow field are described in section 2. Section 3 first presents a survey of the observed bending deformations for the single-bladed rotor, as function of the blade pitch and rotor rotation frequency at constant free-stream velocity, followed by a wider parameter variation, where both the frequency and flow speed are varied. Measurements of the velocity and vorticity fields characterizing the corresponding rotor wake structures are also shown. The overall deformation behaviour of a double-bladed rotor is presented in section 4. Conclusions are given in section 5.

2. Experimental set-up

Experiments were performed in a hydrodynamic channel with a recirculating free-surface water flow and low turbulence intensity (<1%). The dimensions of the test section are: 38 cm width, 50 cm height and 150 cm length; the water height in the channel is 45 cm. The rotor is mounted on a carbon-fibre shaft of 15 mm diameter with an ogive-shaped tip, driven by a stepper motor through a gear box, as shown in Fig. 1(a). Single- and double-bladed rotors of radius $R_0 = 88$ mm were tested. The rotor blade and hub are manufactured separately and assembled for operation. The blade is made of low-density polyethylene (LDPE; density: 1070 g/cm^3, Young's modulus: 3.5 GPa, shear modulus: 2.1 GPa). It has an untwisted rectangular shape of constant chord $c = 20$ mm and its profile is flat, with a constant thickness of 0.7 mm (3% of the chord) and blunt leading and trailing edges. The hub is manufactured from nylon by rapid prototyping. Different rotor pitch angles were tested. For each pitch value, a separate hub was manufactured (this applies to both the single- and double-bladed rotors). The blade is replaced after each set

of experiments, due to the permanent alteration (plastic deformation, breaking) that it may undergo during operation.

The deformations of a flexible blade can be classified into the following types: flapwise bending, parallel to the rotor axis; lead-lag bending, azimuthally in the rotor plane; chordwise deformation, which affects the blade profile geometry (e.g., a change of profile camber sign); and torsion, i.e. the induced blade twist. In this paper, only flapwise bending is considered. Blade torsion is small compared to bending. Measurements of the flow-induced twist for some of the cases shown here can be found in [16]. Lead-lag bending and chordwise deformations are neglected here, due to the high blade stiffness in these directions.

Image processing was used to measure the flapwise deformation. At a given flow condition, a set of images (between 50 and 400) were captured at the same rotor phase. By superposing these phase-locked images (as in Figs. 2 and 6 below), the deformation magnitude and its fluctuation amplitude could be determined by tracking the blade tip position, as shown in section 3.1.

Velocity and vorticity fields around the rotor were measured in a plane containing the rotor axis using two-component Particle Image Velocimetry (PIV). The fluid in the channel was seeded with 10 µm silver-coated glass particles and illuminated using a Nd:YAG pulsed laser (Quantel Twins Ultra 190) positioned below the channel. A high-resolution digital camera (Roper Redlake) was used to record the particle images. The camera was triggered internally for time-averaging (∼200 flow fields recorded at evenly distributed azimuthal blade positions), and by a signal from the stepper motor for phase-averaging (i.e. averaging flow fields at the same blade position). PIV image analysis and post-processing were performed with an in-house MATLAB code [17].

In the following sections, the deformation and flow field measurements of the rotor blades are presented. Initially, the rotor rotation frequency was varied in the range $0 < f < 18$ Hz at a constant free-stream velocity $U_0 = 18$ cm/s. This corresponds to tip speed ratios $\lambda = 2\pi f R_0/U_0 = 0$–$55$, and blade tip Reynolds numbers $Re = 2\pi f R_0 c/\nu = 0$–$2\times10^5$, where ν is the kinematic viscosity of water. Re is proportional to λ in this first series. The blade pitch angle β_0 was varied in the range -10° $< \beta_0 <$ 10°. For two values of the pitch, $|\beta_0| = 2.5°$ and $|\beta_0| = 5°$, in the flow speed and rotation frequency were varied independently, in order to cover a more extended region in the λ–Re parameter space.

For the current set of experiments, involving a single fluid and only one blade material, the Reynolds number and tip speed ratio, which effectively represent the flow velocity and rotor frequency, are sufficient to characterise the various configurations. When the fluid and/or material properties are varied, an additional parameter is required, which pertains to the fluid-structure interaction. One choice for this parameter could be the Cauchy number, i.e. the ratio of the dynamic pressure scale (based on the tip velocity) and the modulus of elasticity of the blade material.

3. One-bladed rotor

3.1. Deformation

Figure 2 shows a series of images where photos captured at the same phase are superposed, for pitch angles $\beta_0 = \pm2.5°$ and $\beta_0 = \pm5°$, at a constant free-stream velocity ($U_0 = 18$ cm/s) and varying rotation frequency f. The choice of these pitch values among the range of angles tested comes from the fact that they are representative for most of the deformation sequences observed in these experiments. Figure 3(a) shows the methodology followed to quantify the flapwise blade deformation. The blade tip positions for all observed deformations are found to approximately lie on a circle whose centre is shifted radially outward by ∼2 cm from the rotor axis. The blade deformation magnitude is represented by the angular coordinate θ. The mean values θ_M and fluctuation amplitudes θ_A of this magnitude for all tested blades are collected in Figs. 3(b,c) and 4; they are discussed in the following.

The deformation sequence for the blade with $|\beta_0| = 2.5°$ in Fig. 2(a) starts with a very slight

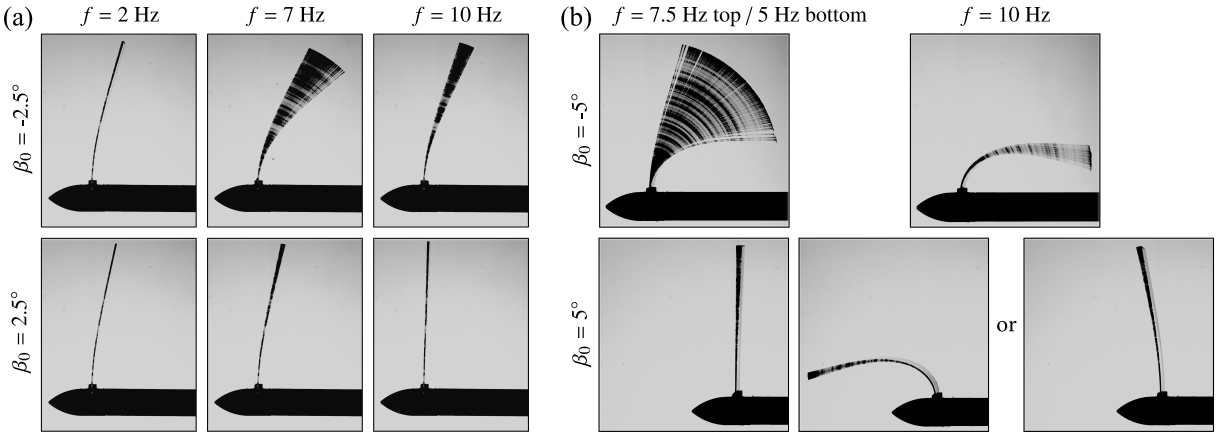

Figure 2. Flapwise deformation of the blades with (a) $|\beta_0| = 2.5°$ and (b) $|\beta_0| = 5°$, as function of the rotation frequency. Superpositions of phase-locked images.

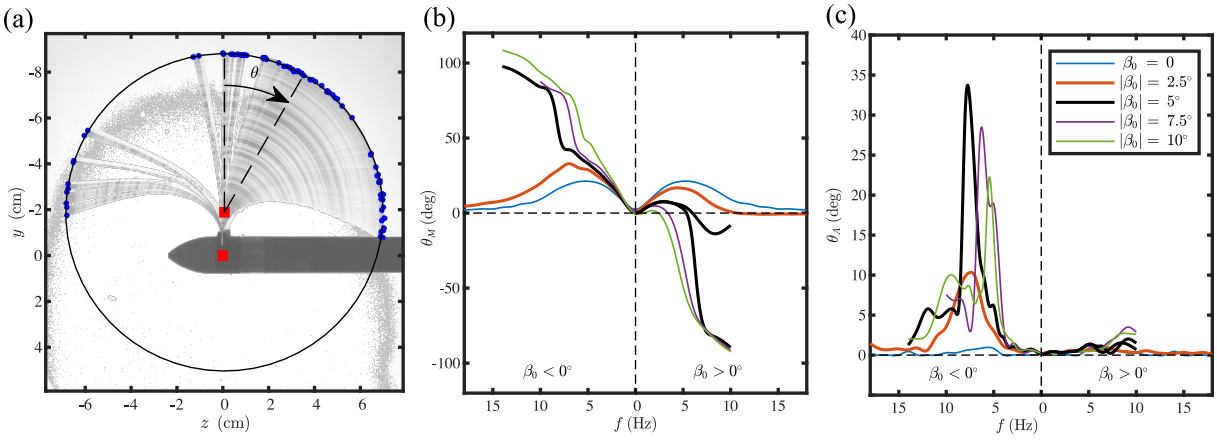

Figure 3. (a) Illustration of the method used to characterise the magnitude of the flapwise blade deformations. (b) Mean deflection θ_M and (c) amplitude θ_A of the deformation fluctuation, for all single-bladed rotors tested at constant free-stream velocity.

flapwise deformation in the downstream direction at $f = 0$, caused by the drag from the free stream. For both negative and positive pitch angles, the magnitude of the blade deflection in the downstream direction increases with the rotation frequency. At $f \approx 5$–7 Hz, the deformation reaches a maximum value (see Fig. 3b). At higher values, the deflection decreases again towards the original unbent state. Interestingly, the blade with negative pitch displays unsteady low-frequency fluctuations, with a maximum amplitude $\theta_A \approx 10°$ at $f = 7$ Hz (Fig. 3c). A similar overall behaviour is witnessed for the blade with $\beta_0 = 0°$.

The deformation sequence for the blade with $|\beta_0| = 5°$ in Fig. 2(b) is significantly different from the one for the lower-pitch blades. In particular, the behaviour differs qualitatively for positive and negative pitch. For $\beta_0 = -5°$, the blade deforms in the downstream direction. The deflection magnitude increases with rotation frequency, reaching extreme deformation states where the blade tip almost touches the mounting shaft, and where the blade cross section is subjected to high stresses, especially near the root. Rotors operating in these extreme conditions over a longer period eventually break. Similar to the $\beta_0 = -2.5°$ case, the blade fluctuates unsteadily, but with a higher maximum amplitude, reaching $\theta_A \approx 35°$ at $f = 7.5$ Hz. As shown in Figs. 3(b,c), the blades with higher pitch values ($|\beta_0| = 7.5°$ and $10°$) qualitatively follow the

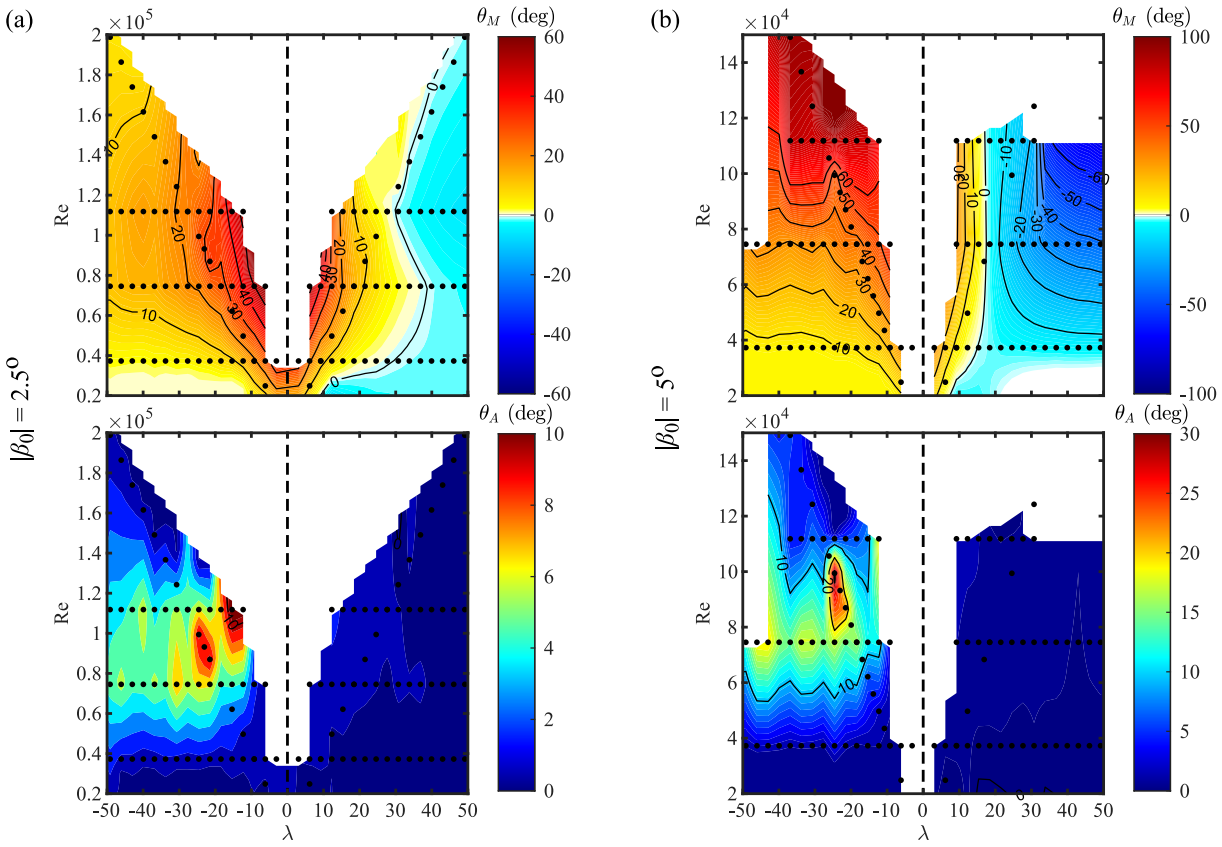

Figure 4. Flapwise deformation contours, function of Re and λ, for blades with (a) $|\beta_0| = 2.5°$ and (b) $|\beta_0| = 5°$. The upper row shows the mean deflection θ_M, and the lower row the fluctuation amplitude θ_A. The dots represent the measured cases.

same deformation sequence.

The particular case with positive pitch $\beta_0 = 5°$ showed an interesting behaviour. Two distinct deformation sequences were observed when the experiments were repeated several times under the same conditions; they are illustrated in Fig. 2(b) (at $f = 10$ Hz) and by the two black lines representing this pitch on the left side of Figs. 3(b,c). The two sequences have a common pattern at low rotation frequency. The blade initially deforms downstream, reaching a maximum at $f = 2$ Hz, and then returns almost to the original unbent state at $f = 5$ Hz. When increasing the rotation frequency further, the blade now deforms in the upstream direction (i.e. the bending direction is reversed), up to a point where two distinct behaviours start to appear. In one case, the blade continues to deform in the upstream direction, reaching extreme deformation states. Blades with higher positive pitch ($\beta_0 = 7.5°$ and $10°$) deform similarly to this sequence, but with the change in bending direction at lower rotation frequencies. In the other case (which was observed more frequently), the blade reverses its deformation trend a second time, and tends to straighten out again at high frequencies, similarly to the low-positive-pitch cases. These results seem to indicate that the pitch value $|\beta_0| = 5°$ represents a limit between low- and high-pitch behaviour in this set of experiments. These two regimes can be identified quite clearly by the two families of curves representing the mean deformation in Fig. 3(b).

The previous results were obtained for a constant free-stream velocity, which means that the non-dimensional tip speed ratio and tip Reynolds number are linked. In order to extend the fluid-structure interaction survey, a second set of experiments was carried out with one-bladed

rotors of pitch angles $|\beta_0| = 2.5°$ and $5°$, where these two parameters were varied independently. The results concerning the mean and fluctuations of the blade deformations are shown in the contour plots of Fig. 4. The sign of the tip speed ratio is here taken to be the same as the one of the pitch. In fact, for a symmetric (rectangular) blade, a negative pitch is equivalent to a rotation in the opposite direction, i.e. with a negative frequency f, which formally gives a negative λ.

Figure 4(a) shows that for the low-pitch blade ($|\beta_0| = 2.5°$), a similar overall deformation behaviour exists at negative and positive tip speed ratios, which is consistent with the previous observations above (Figs. 2a and 3b). The deformation is strongest at low $|\lambda|$. At high positive λ, the blade reverses its deformation direction from downstream to upstream with a relatively small deformation magnitude. A general observation is that the mean deformation θ_M is strongly dependent on λ, whereas Re has weaker effect for this low-pitch blade. However, the amplitude θ_A of the unsteady fluctuations, which only appears for negative λ, has a stronger dependency on Re than on λ. The fluctuations occur in the range $Re = 0.5$–1.5×10^5, with a maximum amplitude of $\theta_A \approx 10°$. For a a more precise characterisation of the effect of tip speed ratio and Reynolds number on the blade fluctuations, more measurement points would be needed within the region of fluctuations.

As before, the blade representing the high-pitch regime ($|\beta_0| = 5°$) shows a different behaviour at negative and positive λ (Fig. 4b). For negative λ, both the deformation magnitude θ_M and fluctuation amplitude θ_A are strongly dependent on Re. At high Re, very strong deformations exist resembling the extremely bent blade case shown in Fig. 2(b) at $f = 10$ Hz. Strong fluctuations again exist in the range $Re = 0.5$–1.5×10^5, but with larger amplitudes. For positive λ, the variation of λ has the dominant effect on the deformation behaviour of the blade, compared to the influence of Re, which is only significant at the highest tip speed ratios. In addition, the blade changes the deformation direction from downstream to upstream at nearly the same tip speed ratio ($\lambda \approx 15$), regardless of the Reynolds number, whereas for the low-pitch blade this change occurs at higher values that vary with Re.

The observed deformation behaviour for low- and high-pitch blades can to some extent be understood by considering the fluid forces acting on them. The magnitude of these forces (lift and drag) depends on the relative flow velocity W and the effective angle of attack α (see Fig. 1b), while their direction depends only on α. The effective angle of attack is related to the pitch angle β_0, the local induced twist angle γ and the flow angle φ at a given blade section as follows:

$$\alpha = \beta_0 + \gamma - \varphi. \tag{1}$$

Both W and α depend on the total axial velocity U and azimuthal velocity V, which result from the free-stream velocity, the blade rotation speed at a given radius and the respective rotor-induced velocities. As the tip speed ratio increases, the flow angle φ decreases and eventually becomes negligible compared to the pitch and induced twist angles near the blade tip. If, in addition, the twist is small (see [16]), this means that the effective angle of attack at high tip speed ratios is mainly determined by the blade pitch. This explains the strong streamwise deformations observed for high-pitch blades at high Reynolds number, due to the fact that the fluid forces increase proportionally to the square of the relative velocity. For low pitch angles, the fact that the blades straighten again at high tip speed ratios indicates that the effective angle of attack must be close to zero, i.e. that the small pitch is compensated by the angle of the induced flow and/or the blade twist, which appears not to be possible at higher pitch. In most of the experiments, i.e. for the cases where the blade is not strongly deformed and no large-scale recirculation is present in its wake, the total axial velocity in the rotor plane near the tip is positive (see section 3.2 below). This means that the contribution from the flow angle to the effective angle of attack is negative. For negative pitch, this enhances the magnitude of the angle of attack, while for positive pitch, the interplay between pitch, twist and flow angle can lead to

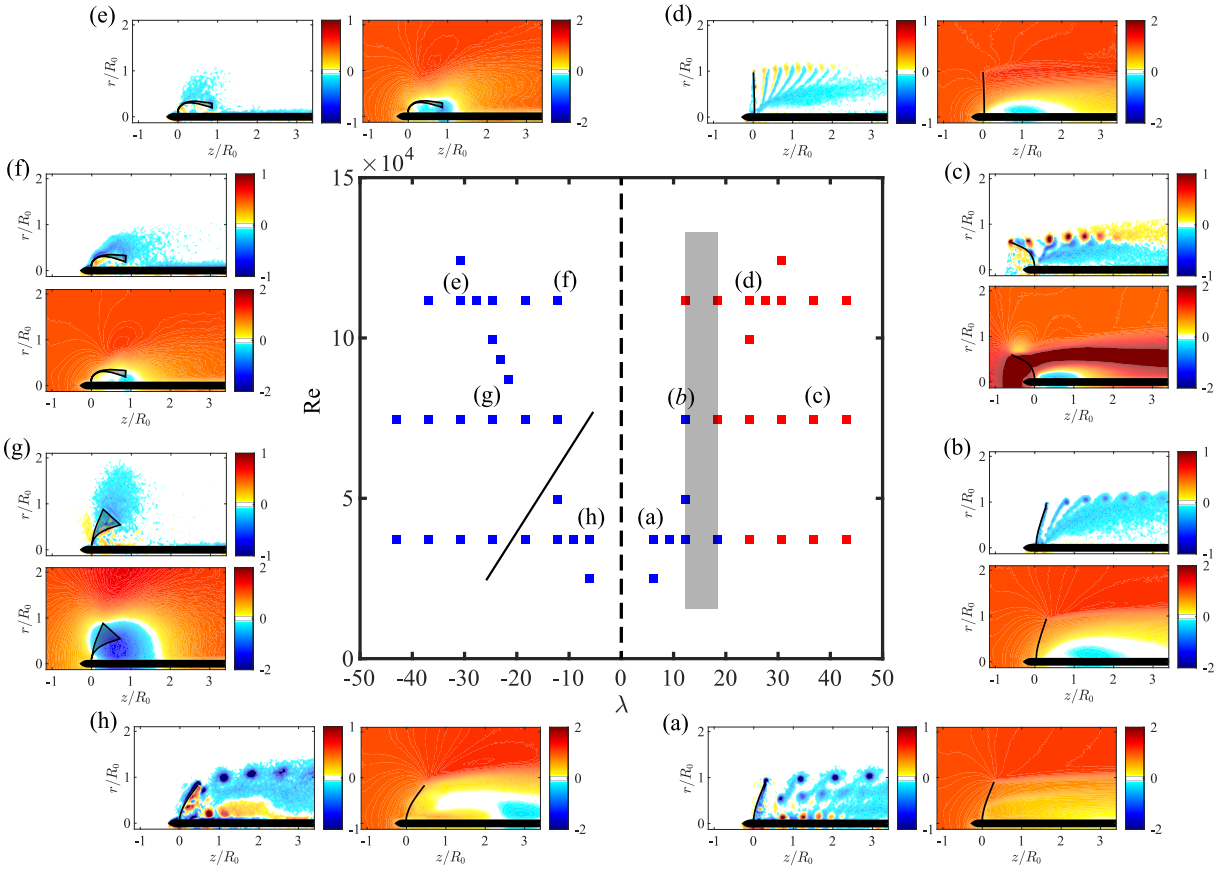

Figure 5. Wake characteristics map for the $|\beta_0| = 5°$ blade, where the marker colour depends on the sign of the vorticity trailing from the blade tip. The chosen cases are represented by the phase-averaged azimuthal vorticity $\omega/(2\pi f)$ and the time-averaged axial velocity U/U_0.

a change of sign of the effective angle of attack, as the rotation rate is increased, resulting in a reversal of the deformation trend.

The above considerations provide a qualitative explanation for the observed mean deformation patterns. Regarding the low-frequency bending fluctuations, they are caused by temporal variations in the fluid forces acting on the blades, resulting from the shedding of a large recirculation zone, as discussed in the following section.

3.2. Wake flow

Flow field measurements in a plane containing the rotor axis were carried out using Particle Image Velocimetry. Figure 5 illustrates the wake properties of the one-bladed rotor with $|\beta_0| = 5°$, as function of Re and λ. The symbols represent all measured cases, with their colour indicating the sign of the vorticity trailing from the blade tip: red for clockwise and blue for anticlockwise rotation. For a representative set of parameter combinations, the distributions of the phase-averaged azimuthal vorticity (ω) and the time-averaged total axial velocity (U) are shown.

At low tip speed ratio and Reynolds number (Fig. 5a and h), the blade is bent downstream with moderate upstream flow induction. The vorticity field for these cases shows three distinct vortices being shed along the rotor plane: one at the tip, the second near mid-span and the third at the root. The presence of multiple vortices with same sign indicates a sharp change in bound

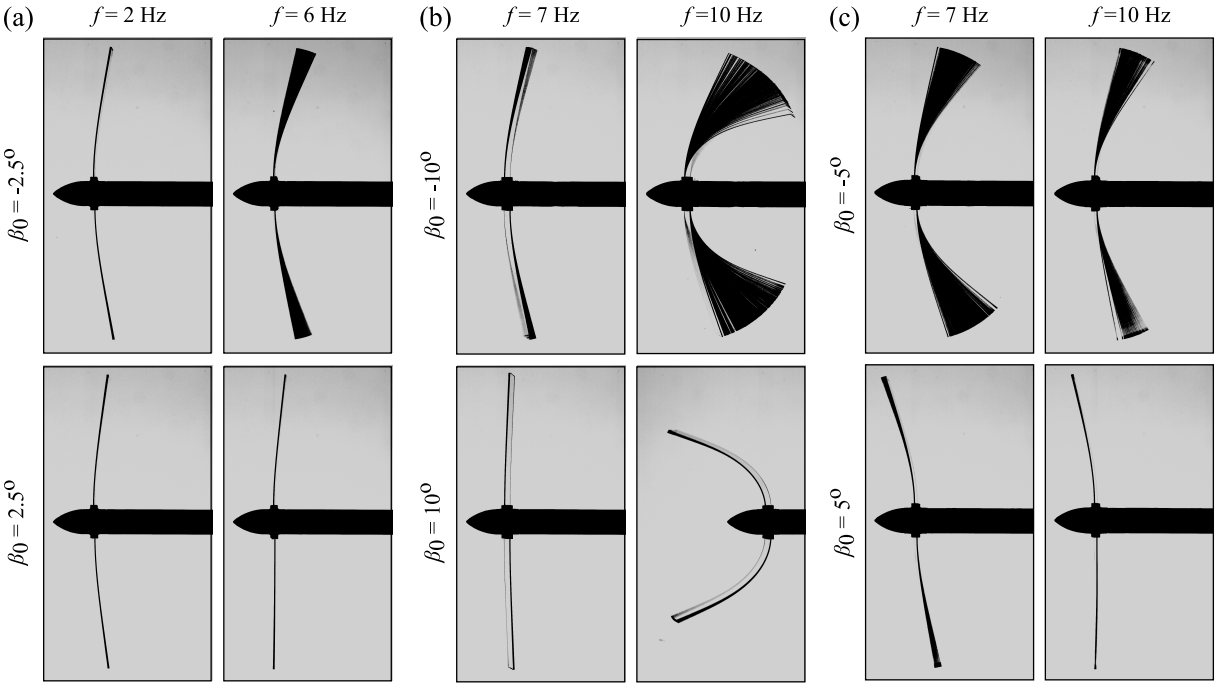

Figure 6. Flapwise deformation of the 2-bladed rotor with (a) $|\beta_0| = 2.5°$, (b) $|\beta_0| = 10°$ and (c) $|\beta_0| = 5°$, as function of rotational frequency. Superposition of phase-locked images.

circulation along the blade span.

For negative λ, as its absolute value grows, the upstream induction of the rotor increases and eventually exceeds the free-stream velocity, which leads to a strong wake expansion and the formation of a large-scale recirculation zone behind the rotor (Fig. 5g). The flow is no longer periodic with the rotor frequency; the recirculation zone is unsteady, exhibiting low-frequency fluctuations which are similar to those found in the Vortex Ring State of the flow around a helicopter rotor during rapid descent [18]. The time scale of these fluctuations is related to the shedding of the ring-shaped recirculation zone, which is at the origin of the observed bending oscillations. A more detailed analysis of this behaviour can be found in [16]. This flow pattern is found for all tested pitch angles at sufficiently negative λ (on the right side of the black solid line in Fig. 5). For high Re, the deformation increases up to extreme downstream bending, as indicated before, at which the recirculation region size and strength decrease considerably (Fig. 5f and e).

For increasing positive λ, the negative axial velocity induction near the blade tip decreases in magnitude, and eventually changes sign around $\lambda \approx 10$–20 (marked by the grey region in Fig. 5), becoming increasingly positive at higher λ (Fig. 5c). This is reflected by the change of the direction of blade bending from downstream to upstream (Fig. 4b). For cases where the blade is strongly bent upstream (Fig. 5c), a very strong downstream induction (more than twice the free stream velocity) is found in the region enclosed by the blade and in the rotor wake.

4. Two-bladed rotor

In this section, we present first results concerning the deformations of a two-bladed flexible rotor. The blade geometry is the same as for the one-bladed rotor in the previous section, and experiments were again carried out at constant free-stream velocity ($U_0 = 18$ cm/s) over a similar range of pitch angles and rotation frequencies.

The overall deformation pattern of the double-bladed rotor is very similar to that of the

single-bladed rotor, as can be seen by comparing the visualisations in Fig. 6 with those of Fig. 2. Low-pitch rotors (Fig. 6a) deform in the downstream direction, reach a maximum deflection, and then straighten out again at high frequencies. High-pitch rotors (Fig. 6b) deform downstream all the way for negative pitch angles or perform the direction change from downstream to upstream for positive pitch angles. In addition, the fluctuations are also witnessed for the two-bladed rotor at negative pitch.

The two-bladed rotor with intermediate blade pitch ($|\beta_0| = 5°$, Fig. 6c), exhibits an interesting behaviour. For the single-bladed rotor, this pitch value was shown to produce deformation patterns related to both low- and high-pitch regimes. Overall, the two-bladed rotor is found to behave according to the low-pitch regime, i.e. at high rotation frequencies, the bending relaxes and the blades straighten out again. Whereas for negative pitch the deformations of the two blades are symmetric, various asymmetric states can be observed for positive pitch. This appears to be related to the fact that the effective angle of attack at the blade tip is close to zero at high frequencies, as discussed above for the single blade. Small asymmetries in the hub geometry or rotor mounting can lead to small angles of attack of opposite sign, which result in deformations in opposite directions. In some cases, one blade was seen to deform even more strongly upstream, which is a sign of high-pitch behaviour. It therefore appears that the double-bladed rotor with pitch $|\beta_0| = 5°$ can also exhibit patterns of both regimes, which can actually occur simultaneously–one on each blade. Further experiments with a better-controlled symmetry between the blades, as well measurements of the wake flow, are needed to fully characterise the deformation behaviour of flexile rotors with more than one blade.

5. Conclusions

We have investigated the fluid-structure interaction of a generic flexible rotor in water, where the large fluid forces can lead to strong blade deformations, focussing on flapwise bending. We have illustrated the effects of varying blade pitch angle, rotation frequency and free stream velocity, and presented a comparison between the deformation behaviour of single- and double-bladed rotors.

The observed deformation patterns for a single-bladed rotor can be separated into two regimes, for low and high pitch angle of the blade. For low pitch, the blade deformation initially grows with increasing tip speed ratio, before reaching a maximum and returning to an almost unbent condition at high values. The dependence on the tip Reynolds number is weak in this regime. For high pitch, the Reynolds number dependence dominates the behaviour, characterised by extreme downstream and upstream bending for high values, at negative and positive pitch, respectively.

In both regimes, strong upstream induction is found for negative pitch (or, equivalently, negative tip speed ratio) and intermediate Reynolds numbers. As shown by flow field measurements, this leads to large recirculation zones in the wake of the rotor, which are unsteady and cause a low-frequency fluctuation of the bending deformation. For positive pitch, both regimes also exhibit a change of direction of the blade bending, as the tip speed ratio is increased, accompanied by a change of sign of the vorticity trailing from the blade tip. This can be understood by considering the evolution of the effective angle of attack of the blade.

The comparison with the deformation patterns found for a two-bladed rotor showed a strong correlation with the one-bladed case, concerning low- and high-pitch regimes. In addition, an interesting case of deformation asymmetry was found for an intermediate pitch angle at high rotation frequency, where the two blades deform with different magnitudes or in opposite directions. This appears to be due to the sensitivity to small differences in the pitch angle of each blade, for cases where the effective angle of attack approaches zero.

This study represents an exploration of the fluid-structure interaction of a moderately flexible rotor operating in a high-density fluid, which revealed interesting deformation behaviours and

wake structures. This work is essentially of a fundamental nature, but it relates to various regimes of rotor operation found in applications like wind or hydrokinetic turbines, and helicopters or drones. Further investigations will focus on the twist deformation of the blades, which has a strong impact on rotor performance, and its effect on the wake. Modelling of the presented interactions of the flexible rotor, which would enable time-efficient parameter and optimisation studies, presents an additional challenge. The results shown in this article may help with the validation of such modelling efforts.

Acknowledgments

The authors are grateful to Éric Bertrand for his assistance with the development of the experimental set-up. This work was supported by the Excellence Initiative of Aix-Marseille University – A*MIDEX, a French *Investissements d'Avenir* programme, in the framework of the Labex MEC.

References

[1] Zhu X, Chen J, Shen X and Du Z 2019 *ASME. J. Sol. Energy Eng.* **141**(041002)
[2] Winston M M 1968 Technical Report NASA/TN D-4820 National Aeronautics and Space Administration
[3] Winston M M 1968 Technical Report NASA/TN D-4465 National Aeronautics and Space Administration
[4] MacPhee D W and Beyene A 2015 *Energy* **90** 1055
[5] Cognet V, Courrech du Pont S, Dobrev I, Massouh F and Thiria B 2017 *Proc. R. Soc.* A **473** 20160726
[6] Sicard J and Sirohi J 2012 *J. Aircraft* **49** 1306
[7] Lv P, Prothin S, Mohd-Zawawi F, Bénard E, Morlier J and Moschetta J M 2015 *J. Fluids Struct.* **55** 25
[8] Siddall R and Kovač M 2014 *Bioinspir. Biomim.* **9** 031001
[9] Yang X, Wang T, Liang J, Yao G and Liu M 2015 *Progr. Aerosp. Sci.* **74** 131
[10] Tan Y H, Siddall R and Kovac M 2017 *IEEE Robot. Autom. Lett.* **2** 1304
[11] Güney M S and Kaygusuz K 2010 *Renew. Sust. Energ. Rev.* **14** 2996
[12] Yuce M I and Muratoglu A 2015 *Renew. Sust. Energ. Rev.* **43** 72
[13] Porter K E et al 2020 *J. Fluids Struct.* **93** 102825
[14] Mycek P, Gaurier B, Germain G, Pinon G and Rivoalen E 2013 *Int. J. Mar. Energy* **1** 70
[15] Gotelli C, Musa M, Guala M and Escauriaza C 2019 *Energies* **12**
[16] Eldemerdash A S and Leweke T 2021 *J. Fluids Struct.* In press
[17] Meunier P and Leweke T 2003 *Exp. Fluids* **35** 408
[18] Leishman J G 2006 *Principles of Helicopter Aerodynamics* (Cambridge: CUP)